Images of molecular orbitals in strong-field photoelectron momentum distributions generated by circularly polarized pulses

Vinh N. T. Pham,[1,2] Oleg I. Tolstikhin,[3] and Toru Morishita[2]

[1]*Department of Physics, Ho Chi Minh City University of Education, Ho Chi Minh City 748342, Vietnam*

[2]*Institute for Advanced Science, The University of Electro-Communications, 1-5-1 Chofu-ga-oka, Chofu-shi, Tokyo 182-8585, Japan*

[3]*Moscow Institute of Physics and Technology, Dolgoprudny 141700, Russia*

(Received 25 November 2018; published 23 January 2019)

Strong-field photoelectron momentum distributions (PEMDs) generated in the ionization of molecules by circularly polarized laser pulses contain valuable information on the structure of the ionizing molecular orbital. In this paper, we investigate using the adiabatic theory how this information is imprinted in and can be extracted from such PEMDs. The PEMDs have a donutlike shape. The variation of a PEMD along the donut reproduces the orientation dependence of the ionization rate of the ionizing orbital, and hence reflects its nodal structure and shape. The transverse structure of the PEMD in cross sections of the donut corresponding to orientations of the molecule at which the ionizing orbital has a node in the direction opposite to that of the instantaneous laser field reflects the interplay of two competing ionization channels, which provides additional information on the orbital structure. We illustrate these features by the analysis of PEMDs for three states of different symmetries of the hydrogen molecular ion H_2^+.

DOI: 10.1103/PhysRevA.99.013428

I. INTRODUCTION

Extracting target structure and dynamics information from high-order harmonic spectra and photoelectron momentum distributions (PEMDs) generated in the ionization of atoms and molecules by intense low-frequency laser pulses is one of the fundamental goals of strong-field physics [1]. In high-order harmonic spectroscopy, a powerful technique of tomographic imaging of molecular orbitals is established [2]; for a review of its developments, see Ref. [3]. Photoelectron spectroscopy suggests several complementing approaches of two kinds, depending on whether rescattered or direct photoelectrons perform imaging. Rescattered photoelectrons recollide with the parent ion before arriving at a detector [4], so their contribution to strong-field PEMDs bears information on the target collisional properties. One widely used approach in rescattering photoelectron spectroscopy focuses on the high-energy part of PEMDs dominated by nearly backward rescattered photoelectrons [5] and enables one to extract the differential cross section for elastic scattering of a photoelectron on the parent ion [6,7]; a review of this approach and its applications is given in Ref. [8]. Recently, the theoretical foundation of this approach has been revisited [9] which made the extraction procedure quantitative [10]. Another promising approach focuses on a holographic pattern in the intermediate-energy part of PEMDs resulting from interference of direct and nearly forward rescattered photoelectrons [11], which encodes information on the phase of the electron-ion elastic scattering amplitude [12]. The potentiality of this approach for resolving electronic dynamics on the attosecond timescale was demonstrated in Ref. [13]. The contribution of direct photoelectrons to PEMDs contains information on the tunneling ionization process and, through this, on the ionizing orbital. While in rescattering photoelectron spectroscopy linearly polarized laser pulses are usually used, to force a photoelectron to return to the parent ion for recollision, for the observation of direct photoelectrons it is preferable to use circularly polarized pulses to eliminate rescattering [14] which contaminates tunneling observables. Thus, circular polarization is essential for accurate measurements of tunneling ionization rates of molecules [15–19]. Donut-shaped strong-field PEMDs generated by circularly polarized pulses are being intensively studied, both experimentally and theoretically, as a source of information on molecular orbitals [20–39]. In this paper, we analyze images of the ionizing orbital which can be extracted from such PEMDs on the basis of the adiabatic theory [40].

Within the adiabatic theory, the PEMD generated by a circularly polarized pulse is expressed analytically in terms of properties of a Siegert state (SS) [41–43] originating from the initial electronic state in the presence of a static electric field equal to the instantaneous laser field. If the laser field is not too strong, so that ionization occurs in the tunneling (under-the-barrier) regime, then the properties of the SS needed can be expressed in terms of properties of the unperturbed initial state using the weak-field asymptotic theory (WFAT) [44]. This is how an image of the ionizing orbital is imprinted in the PEMD. The adiabatic theory is quantitative, its predictions converge to the exact results as the laser frequency decreases. This has been demonstrated by comparison with accurate results obtained by solving the time-dependent Schrödinger equation (TDSE) for atomic targets [9,40,45]. Most of the TDSE treatments for molecular targets interacting with low-frequency circularly polarized laser pulses to date are restricted to two-dimensional models [25,28,31,34,39]; we are aware of only a few such calculations of PEMDs for realistic three-dimensional systems [35–38]. In this situation,

 ©2019 American Physical Society

predictions of the adiabatic theory may prove to be very useful. Here, we illustrate application of the theory to molecules by calculating and analyzing PEMDs for three states of different symmetries of the hydrogen molecular ion H_2^+.

The paper is organized as follows. In Sec. II, we summarize equations defining the PEMD generated by a circularly polarized pulse within the adiabatic theory [40]. In Sec. III, the quantitative performance of these equations is illustrated by comparing the adiabatic results with the TDSE results for the hydrogen atom in the ground state. In Sec. IV, the adiabatic theory is applied to the analysis of PEMDs for the ground ($1s\sigma$) and two excited ($2p\sigma$ and $2p\pi^+$) states of H_2^+. The manifestation of the structure of the ionizing orbital in the PEMDs is discussed by means of the WFAT [44]. Section V concludes the paper.

II. ADIABATIC THEORY

We consider an atom or molecule treated in the single-active-electron approximation interacting with an intense low-frequency laser pulse. The TDSE in the dipole approximation and length gauge reads as (atomic units are used throughout)

$$i\,\frac{\partial\psi(\mathbf{r},t)}{\partial t} = \left[-\tfrac{1}{2}\Delta + V(\mathbf{r}) + \mathbf{F}(t)\mathbf{r}\right]\psi(\mathbf{r},t), \qquad (1)$$

where the potential $V(\mathbf{r})$ describes the interaction of the active electron with the parent ion and $\mathbf{F}(t)$ is the electric field of the pulse. The field is presented in the form $\mathbf{F}(t) = F(t)\mathbf{e}(t)$, where $F(t) \geqslant 0$ is the field strength and $\mathbf{e}(t)$ is the polarization vector satisfying $\mathbf{e}^2(t) = 1$. In this paper, we consider pulses with a Gaussian envelope

$$F(t) = F_0 \exp[-(2t/T)^2], \qquad (2)$$

propagating along the z axis and circularly polarized in the (x, y) plane

$$\mathbf{e}(t) = \mathbf{e}_x \cos\omega t + \mathbf{e}_y \sin\omega t, \quad \omega = 2\pi n_{\rm oc}/T. \qquad (3)$$

Thus, a pulse is characterized by its amplitude F_0, duration T, frequency ω, and the number of optical cycles $n_{\rm oc}$. For reference, $F_0 = 0.1$ corresponds to the intensity $I \approx 7.02\times10^{14}$ W/cm^2 and $\omega = 0.057$ corresponds to the wavelength $\lambda \approx 800$ nm. The initial condition for Eq. (1) is

$$\psi(\mathbf{r}, t \to -\infty) = \phi_0(\mathbf{r})e^{-iE_0t}, \qquad (4)$$

where E_0 and $\phi_0(\mathbf{r})$ are the energy and wave function of a bound state of the unperturbed system. The main observable of interest here is the PEMD defined by

$$P(\mathbf{k}) = |I(\mathbf{k})|^2, \quad I(\mathbf{k}) = \langle\psi_{\mathbf{k}}^{(-)}|\psi(t\to\infty)\rangle, \qquad (5)$$

where $I(\mathbf{k})$ is the ionization amplitude and $|\psi_{\mathbf{k}}^{(-)}\rangle$ is the scattering *out* eigenstate of the field-free Hamiltonian with the asymptotic momentum $\mathbf{k}$ normalized by $\langle\psi_{\mathbf{k}}^{(-)}|\psi_{\mathbf{k}'}^{(-)}\rangle = (2\pi)^3\delta(\mathbf{k}-\mathbf{k}')$ [46,47]. We solve Eq. (1) using a method described in Ref. [48] generalized to the circular polarization case. The TDSE results reported below are obtained from Eq. (5).

Let $T_0 = \min(T, 2\pi/\omega)$ be the characteristic time of the laser field and ΔE denote the energy spacing between the initial state and the nearest eigenstate of the unperturbed system. The adiabatic parameter $\epsilon = 2\pi/\Delta E T_0$ gives the ratio of the electronic and laser field timescales. Small values of this parameter correspond to the adiabatic regime. The adiabatic theory [40] amounts to the asymptotic solution of Eq. (1) for $\epsilon \to 0$. Within this theory, the ionization amplitude is obtained in the form $I(\mathbf{k}) = I_a(\mathbf{k}) + I_r(\mathbf{k})$, where the adiabatic $I_a(\mathbf{k})$ and rescattering $I_r(\mathbf{k})$ parts represent contributions from electrons which go directly to a detector after their release from the system and those which experience rescattering before arriving at a detector, respectively. The rescattering part can be neglected in the circular polarization case, so in this paper we consider only the adiabatic part. The leading-order term in the asymptotics of $I_a(\mathbf{k})$ for $\epsilon \to 0$ is given by [40]

$$I_a(\mathbf{k}) = e^{i\pi/4}(2\pi)^{1/2}\sum_i \frac{A(\Delta\mathbf{k}_\perp; t_i)}{F^{1/2}(t_i)} \exp\left[i\mathcal{S}(t_i,\mathbf{k}) - is(t_i)\right]. \qquad (6)$$

This formula contains quantities of two kinds, quantum and classical. The quantum quantities are determined by properties of the SS in an external static electric field $\mathbf{F}$ originating from the initial bound state and satisfying outgoing-wave boundary conditions in the asymptotic region [41–43]. Equation (6) involves the complex SS energy eigenvalue $E(\mathbf{F})$, whose imaginary part defines the ionization rate $\Gamma(\mathbf{F}) = -2\,\mathrm{Im}[E(\mathbf{F})]$, and the transverse momentum distribution (TMD) amplitude $A(\mathbf{k}_\perp;\mathbf{F})$, where $\mathbf{k}_\perp$ is the transverse with respect to $\mathbf{F}$ part of the momentum of electrons in the outgoing flux. The functions $E(\mathbf{F})$ and $A(\mathbf{k}_\perp;\mathbf{F})$ can be calculated using the method developed in Refs. [41–43]; their behavior for the different states in atomic and molecular potentials is illustrated therein. They should be taken at the instantaneous value of the field $\mathbf{F}(t)$, and thus become functions of time denoted by $E(t) = E(\mathbf{F}(t))$ and $A(\mathbf{k}_\perp;t) = A(\mathbf{k}_\perp;\mathbf{F}(t))$. From Eq. (2) we have $E(t\to\pm\infty) = E_0$. The quantum action in Eq. (6) is

$$s(t) = E_0 t + \int_{-\infty}^{t}[E(t') - E_0]\,dt'. \qquad (7)$$

The second term here accounts for both the accumulation of an additional phase by the initial state due to the Stark shift and its depletion via tunneling or over-the-barrier ionization described by the instantaneous ionization rate $\Gamma(t) = -2\,\mathrm{Im}[E(t)] = \Gamma(\mathbf{F}(t))$. Note that in the weak-field limit the rate is related to the TMD amplitude by [44]

$$\Gamma(\mathbf{F}) = \int |A(\mathbf{k}_\perp;\mathbf{F})|^2\,\frac{d\mathbf{k}_\perp}{(2\pi)^2}, \quad F\to 0. \qquad (8)$$

The classical quantities are expressed in terms of the velocity for a reference electron trajectory in the field $\mathbf{F}(t)$:

$$\mathbf{v}(t) = -\int_{-\infty}^{t}\mathbf{F}(t')\,dt', \quad \mathbf{v}(t\to\infty) = \mathbf{v}_\infty. \qquad (9)$$

In the present case $\mathbf{v}_\infty = (v_\infty, 0, 0)$, where

$$v_\infty = -\pi^{3/2}n_{\rm oc}\exp\left(-\frac{\pi^2 n_{\rm oc}^2}{4}\right)v_0 \qquad (10)$$

and $v_0 = F_0/\omega$. The ratio v_∞/v_0 rapidly decreases as $n_{\rm oc}$ grows and is negligibly small for few-cycle pulses considered in the calculations below; for example, $v_\infty/v_0 \approx -5.8\times10^{-4}$ and -3.8×10^{-9} for $n_{\rm oc} = 2$ and 3, respectively. The classical

action in Eq. (6) is

$$\mathcal{S}(t,\mathbf{k}) = \frac{1}{2}\mathbf{k}^2 t - \frac{1}{2}\int_t^\infty \left[\mathbf{u}_i^2(t',\mathbf{k}) - \mathbf{k}^2\right] dt', \tag{11}$$

where

$$\mathbf{u}_i(t,\mathbf{k}) = \mathbf{k} - \mathbf{k}_a(t) \tag{12}$$

and

$$\mathbf{k}_a(t) = \mathbf{v}_\infty - \mathbf{v}(t). \tag{13}$$

The vector $\mathbf{u}_i(t,\mathbf{k})$ gives the initial velocity with which an electron driven by the field should start its motion at time t to have the final velocity after the end of the pulse equal to $\mathbf{k}$. The moments of ionization are defined by

$$\mathbf{e}(t)\mathbf{u}_i(t,\mathbf{k}) = 0 \quad \rightarrow \quad t = t_i(\mathbf{k}), \tag{14}$$

and the summation in Eq. (6) runs over all real solutions to this equation. A curve $\mathcal{K}_a$ in the photoelectron momentum space traced by the end of $\mathbf{k}_a(t)$ as t varies along the real axis represents the classical support of the PEMD. Since $d\mathbf{k}_a(t) = \mathbf{F}(t)dt$, the field $\mathbf{F}(t)$ is tangential to the curve $\mathcal{K}_a$ at the point $\mathbf{k} = \mathbf{k}_a(t)$. In the adiabatic regime, the length of $\mathcal{K}_a$ is $O(\epsilon^{-1})$ and the PEMD $P(\mathbf{k})$ is localized in a narrow pipelike neighborhood K_a of $\mathcal{K}_a$ of width $O(\epsilon^0)$ determined by the width of the TMD. Each $\mathbf{k} \in K_a$ can be presented in the form

$$\mathbf{k} = \mathbf{k}_a(t_i) + \Delta\mathbf{k}_\perp, \tag{15}$$

which defines the first argument of the TMD amplitude in Eq. (6). From Eqs. (12) and (15) we have $\mathbf{u}_i(t_i,\mathbf{k}) = \Delta\mathbf{k}_\perp$, thus, $\Delta\mathbf{k}_\perp$ is the initial velocity of an electron at the moment of ionization t_i and, as follows from Eq. (14), it is orthogonal to the instantaneous field $\mathbf{F}(t_i)$. The adiabatic results reported below are obtained from Eq. (6). They will be denoted by AA, which stands for the adiabatic approximation. Note that Eq. (6) amounts to a simple asymptotics using the terminology of Ref. [45]. In this paper we do not discuss a uniform asymptotics also considered in Ref. [45], which works better at weaker fields. The implementation of the uniform asymptotics would require to calculate the SS at complex field strengths, which is feasible for spherically symmetric atomic potentials but becomes more expensive computationally for molecular potentials of main interest here.

III. PERFORMANCE OF THE ADIABATIC THEORY FOR THE HYDROGEN ATOM

The quantitative performance of the adiabatic theory was demonstrated by comparison with accurate TDSE results for finite-range [40] and Coulomb-tail [9] potentials, in the linear polarization case, and for a finite-range potential [45], in the circular polarization case. It should be noted that the asymptotics of the adiabatic part $I_a(\mathbf{k})$ of the ionization amplitude derived in Ref. [40], particularly Eq. (6), applies to both finite-range and Coulomb-tail potentials, while that of the rescattering part $I_r(\mathbf{k})$ holds only for finite-range potentials. Before we turn to the application of Eq. (6) to a Coulomb-tail molecular potential, for which solving Eq. (1) is beyond our current capabilities, it is worthwhile to illustrate its performance for a Coulomb-tail atomic potential, in which case the

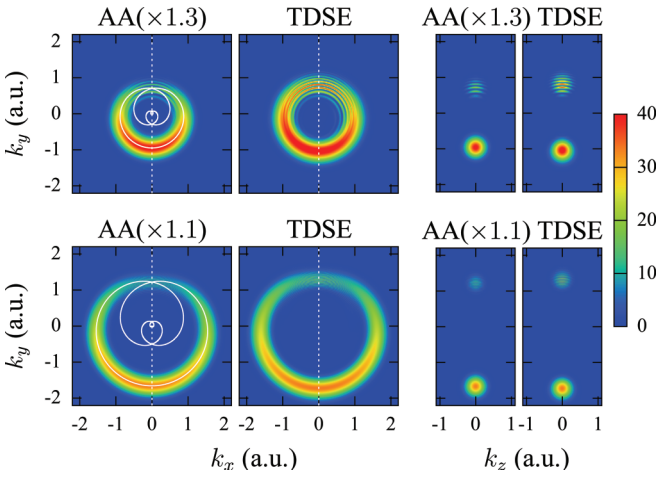

FIG. 1. Two-dimensional cuts of the PEMDs $P(\mathbf{k})$ for H($1s$) in the $(k_x, k_y, k_z = 0)$ (left panels) and $(k_x = 0, k_y, k_z)$ (right panels) planes. The PEMDs are generated by pulses with $F_0 = 0.07$ and $n_{\rm oc} = 2$. In the top panels, $T = 160$ ($\omega \approx 0.079$, $v_0 \approx 0.89$). In the bottom panels, $T = 280$ ($\omega \approx 0.045$, $v_0 \approx 1.56$). The adiabatic results are multiplied by factors indicated in the figure. The solid white lines in the leftmost panels show the curve $\mathcal{K}_a$ traced by the vector (13).

predictions of Eq. (6) can be compared with the TDSE results. The calculations presented in this section extend the validation of the adiabatic theory in the circular polarization case [45] to potentials with a Coulomb tail.

Here, we discuss ionization from the ground $1s$ state of the hydrogen atom described by Eq. (1) with $V(\mathbf{r}) = -1/r$. Because of the spherical symmetry of the potential and the initial state, the corresponding SS energy eigenvalue $E(F)$ and TMD amplitude $A(k_\perp; F)$ needed to implement Eq. (6) do not depend on the orientations of the external electric field $\mathbf{F}$ and the transverse momentum $\mathbf{k}_\perp$ of an ionized electron; the behavior of these functions is illustrated in Ref. [41]. We consider sets of pulses with a fixed amplitude F_0 and the number of optical cycles $n_{\rm oc}$ and growing duration T, therefore decreasing adiabatic parameter $\epsilon \propto 1/T$. The adiabatic theory [40] predicts that the AA results from Eq. (6) should converge to the TDSE results from Eq. (5) as T grows. The goal of the calculations is to demonstrate this convergence.

The AA and TDSE results for PEMDs generated by two-cycle pulses with $F_0 = 0.07$ and two durations $T = 160$ and 280 are shown in the top and bottom panels of Figs. 1 and 2, respectively. In Fig. 1, two-dimensional cuts of the PEMDs in the $(k_x, k_y, k_z = 0)$ and $(k_x = 0, k_y, k_z)$ planes are compared. The PEMDs are seen to have a donutlike shape. The variation of their amplitude along the donut is caused by the finiteness of the number of optical cycles in the pulse, which amounts to the carrier-envelope phase effect. To facilitate the comparison, the adiabatic results for each T are multiplied by a factor indicated in the figure. The factor approaches unity as T grows, which illustrates the convergence of the overall amplitudes of the AA and TDSE PEMDs. The shapes of the AA and TDSE distributions in Fig. 1 also converge as T grows. This is more clearly seen in the one-dimensional cuts of the PEMDs along the k_y axis shown in Fig. 2. The cuts consist of two peaks localized in the intervals where the k_y axis crosses the donut.

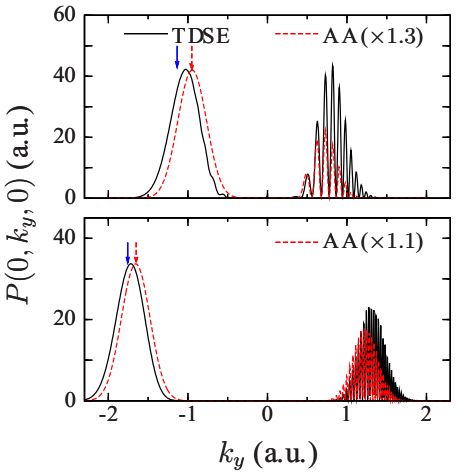

FIG. 2. One-dimensional cuts of the PEMDs shown in Fig. 1 along the dashed white lines (at $k_x = k_z = 0$). The top (bottom) panel corresponds to the top (bottom) panel in Fig. 1. The dashed (red) and solid (blue) arrows indicate the values of $k_{ay}(0)$ and $k^+_{ay}(0)$ defined by Eqs. (13) and (16), respectively.

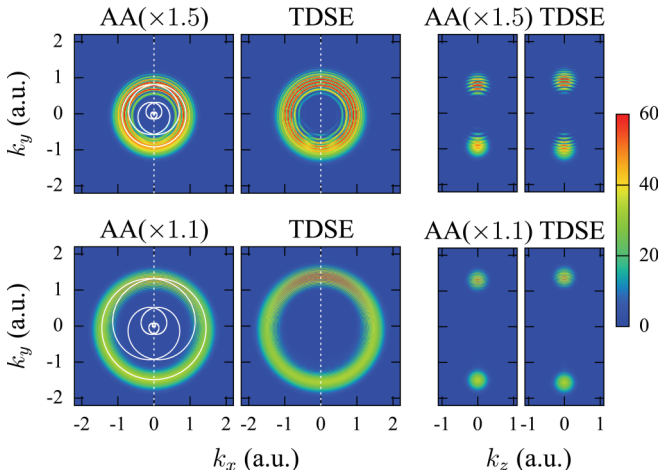

FIG. 3. Two-dimensional cuts of the PEMDs $P(\mathbf{k})$ for H($1s$) in the $(k_x, k_y, k_z = 0)$ (left panels) and $(k_x = 0, k_y, k_z)$ (right panels) planes. The PEMDs are generated by pulses with $F_0 = 0.07$ and $n_{oc} = 3$. In the top panels, $T = 240$ ($\omega \approx 0.079$, $v_0 \approx 0.89$). In the bottom panels, $T = 390$ ($\omega \approx 0.048$, $v_0 \approx 1.45$). The adiabatic results are multiplied by factors indicated in the figure. The solid white lines in the leftmost panels show the curve $\mathcal{K}_a$ traced by the vector (13).

The agreement is better for the left peak, which corresponds to a stronger instantaneous field at the moment of ionization, but it also improves for the right oscillatory peak as T increases. Unfortunately, we cannot extend the comparison to larger T because the TDSE calculations become unfeasible.

A shift between the left peaks in the AA and TDSE results seen in Fig. 2 deserves a discussion. As has been mentioned above, in the adiabatic regime the PEMD $P(\mathbf{k})$ is localized near its classical support $\mathcal{K}_a$ traced by the vector (13). This follows from Eq. (6), because the TMD amplitude $A(\mathbf{k}_\perp; t)$ generally peaks at $\mathbf{k}_\perp = \mathbf{0}$ (a situation where this is not the case is discussed in Sec. IVC). For pulses containing sufficiently many optical cycles, the part of $\mathcal{K}_a$ corresponding to instantaneous field strengths close to the maximum of the envelope (2) forms a circle of radius $v_0 = F_0/\omega$, which results in the donutlike shape of the PEMD. This is confirmed by the distributions shown in Fig. 1, where $\mathcal{K}_a$ is depicted by the solid white lines in the leftmost panels. The lowest point of $\mathcal{K}_a$, where it crosses the k_y axis, corresponds to the maximum of the field strength at $t = 0$ (in fact, the crossing occurs at a small negative t because of the nonzero value of v_∞, but we neglect this difference in the discussion). However, the localization of the PEMD near $\mathcal{K}_a$ holds only in the limit $\epsilon \to 0$. In Ref. [45], by taking into account terms of the first order in ϵ, it was shown that the maximum of the PEMD in the transverse with respect to $\mathcal{K}_a$ direction is shifted from $\mathcal{K}_a$ to a curve $\mathcal{K}^+_a$ traced by the vector

$$\mathbf{k}^+_a(t) = \mathbf{k}_a(t) - \frac{\varkappa^2 \dot{\mathbf{e}}(t)}{6F(t)}, \tag{16}$$

where $\varkappa = \sqrt{2|E_0|}$. The second term in this equation, which is $O(\epsilon^1)$, means that $\mathcal{K}^+_a$ is expanded from $\mathcal{K}_a$ in the radial direction outwards. Equation (6) gives only the leading-order term in the asymptotics of the ionization amplitude for $\epsilon \to 0$, so it does not account for this nonadiabatic effect. Indeed, the maximum of the left peak in the AA results in Fig. 2 is located at $k_y = k_{ay}(0)$, where $\mathcal{K}_a$ crosses the k_y axis; this point is indicated by the dashed (red) arrows. Equation (16) predicts the position of the maximum at $k_y = k^+_{ay}(0) = k_{ay}(0) - \varkappa^2\omega/6F_0$, where $\mathcal{K}^+_a$ crosses the k_y axis; this point is indicated by the solid (blue) arrows. The maximum is thus expected to be shifted to the left by $\Delta k_y = 0.187$ and 0.107 for $T = 160$ and 280, respectively. The peak in the TDSE results is shifted to the left from the AA peak by $\Delta k_y = 0.079$ and 0.058, which amounts to 42% and 54% of the shift predicted by Eq. (16) for the two values of T, respectively. Thus, there exists a nonadiabatic shift of the peak predicted in Ref. [45] and Eq. (16) describes it more accurately as T grows.

Similar results for PEMDs generated by three-cycle pulses with the same amplitude $F_0 = 0.07$ and two durations $T = 240$ and 390 are shown in the top and bottom panels of Figs. 3 and 4, respectively. The structure of the PEMDs and the level of agreement between the AA and TDSE results in this case are similar to those discussed above. The general conclusion supported by these calculations is as follows: The adiabatic results from Eq. (6) converge to the TDSE results as the pulse frequency decreases and at $\omega \sim 0.045$ (corresponding to the wavelength $\lambda \sim 1010$ nm) the difference reduces to $\sim$10%, so the agreement becomes quantitative. This agrees with a conclusion following from calculations for a finite-range potential in Ref. [45]. We note that the rate of convergence of the adiabatic and TDSE results depends on the pulse amplitude and was shown to be higher for stronger fields [45].

Before closing this section, it is instructive to illustrate how the different terms in Eq. (6) representing contributions from the different moments of ionization defined by Eq. (14) affect the shape of the PEMD. For pulses defined by Eqs. (2) and (3), Eq. (14) has infinitely many solutions for each $\mathbf{k}$ inside the pipelike region K_a of localization of the PEMD around its classical support $\mathcal{K}_a$. However, only few of them lying near the maximum of the pulse envelope (2) give non-negligible contributions to Eq. (6). This can be seen from

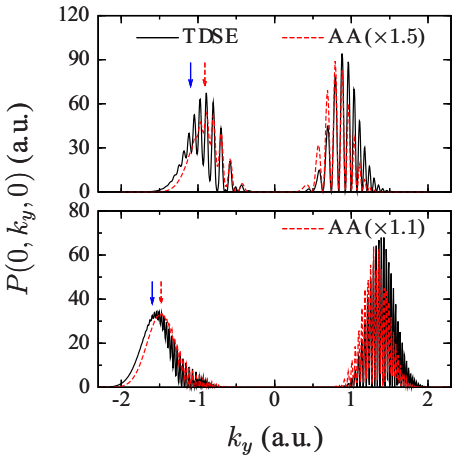

FIG. 4. One-dimensional cuts of the PEMDs shown in Fig. 3 along the dashed white lines (at $k_x = k_z = 0$). The top (bottom) panel corresponds to the top (bottom) panel in Fig. 1. The dashed (red) and solid (blue) arrows indicate the values of $k_{ay}(0)$ and $k^+_{ay}(0)$ defined by Eqs. (13) and (16), respectively.

Eq. (8), which, roughly speaking, means that the magnitude of $A(\mathbf{k}_\perp; t)$ varies with t as $\Gamma^{1/2}(t)$, and the fact that the instantaneous ionization rate $\Gamma(t)$ sharply peaks near the maximum of the field strength $F(t)$. We illustrate this point by considering the pulse used to obtain the results shown in the bottom panels of Figs. 3 and 4. Let us focus on the one-dimensional cut of the PEMD generated by this pulse along the k_y axis shown in the bottom panel of Fig. 4. Several solutions t_i of Eq. (14) contributing to Eq. (6) in this case as functions of k_y are shown in the top panel of Fig. 5. As follows from Eq. (14), for a nearly monochromatic many-cycle pulse with $n_{\rm oc} \gg 1$ the solutions would be given by $t_i = \pm\pi/\omega,\ \pm 3\pi/\omega, \ldots,$ for $k_y > 0$, and $t_i = 0,\ \pm 2\pi/\omega, \pm 4\pi/\omega, \ldots,$ for $k_y < 0$. This explains the behavior of $t_i(k_y)$ at sufficiently large k_y. The finiteness of $n_{\rm oc} = 3$ for the present pulse modifies this behavior at small k_y. The individual contributions of the different solutions of Eq. (14) to the PEMD are shown in the bottom panel of Fig. 5. The dominant contribution to the left peak in the distribution comes from the ionization moment t_2, which is closest to the maximum of the pulse envelope (2). The contributions from t_1 and t_3 (multiplied in the figure by 10) are much smaller, but not negligible, since they are responsible for the appearance of the interference structure seen in the right wing of the peak. The right peak mainly consists of the contributions from t_4 and t_5; they have comparable amplitudes, which results in the high-contrast interference structure. The figure also shows the incoherent sum of all individual contributions, that is, the sum of their absolute values squared, and their coherent sum obtained from Eq. (6), the latter coinciding with the AA results shown in the bottom panel of Fig. 4.

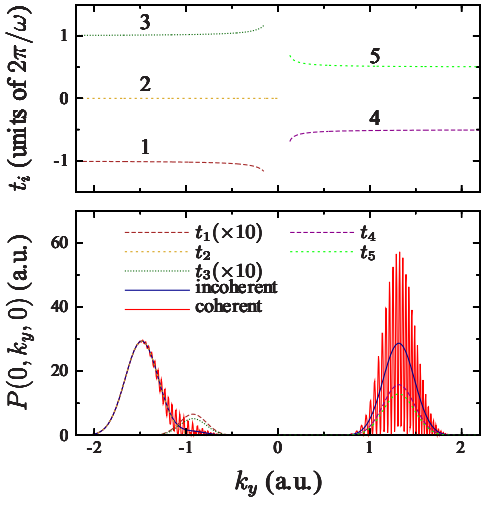

FIG. 5. Top panel: several moments of ionization t_i (in units of the laser period $2\pi/\omega$) defined by Eq. (14) for $\mathbf{k} = (0, k_y, 0)$ as functions of k_y giving non-negligible contributions to Eq. (6). Bottom panel: individual contributions from the corresponding t_i to the PEMD (broken lines, the contributions from t_1 and t_3 are multiplied by 10) and their incoherent (smooth solid blue line) and coherent (oscillatory solid red line) sums. The results correspond to the pulse used in the bottom panel of Fig. 4.

The phase of the different terms in Eq. (6) is thus seen to determine the interference structure of the PEMD. This phase consists of the classical action (11), the real part of the quantum action (7), and the phase of the TMD amplitude. As the number of optical cycles $n_{\rm oc}$ in the pulse grows, a series of above-threshold ionization peaks separated by the photon energy ω emerges from the interference structure. To illustrate this feature, we have calculated using Eq. (6) the PEMD for H($1s$) generated by a 15-cycle pulse with $F_0 = 0.07$ and $T = 1650$ ($\omega \approx 0.057$ corresponding to $\lambda \approx 800$ nm). The one-dimensional cut of the PEMD along the k_y axis (similar to the cuts shown in Figs. 2 and 4) is presented in Fig. 6. In the top panel, the PEMD is shown as a function of the photoelectron momentum k_y. Both peaks in this case have a rapidly oscillating substructure caused by the interference of the different terms in Eq. (6) (compare with Figs. 2 and 4). In the bottom panel, the same PEMD in the interval $1 \leqslant k_y \leqslant \sqrt{1.6}$ is replotted as a function of the photoelectron energy $k_y^2/2$. This reveals a series of above-threshold ionization peaks. As can be seen from Eq. (6), for a nearly monochromatic pulse ($n_{\rm oc} \gg 1$) the peaks would be located at energies $k_y^2/2 = {\rm Re}[E(F_0)] - v_0^2/2 + n\omega$ corresponding to absorption of n photons, with the Stark shift of the initial state and a ponderomotive shift of the ionization threshold taken into account. These energies are shown by the vertical dashed lines in the bottom panel of Fig. 6. In the present case, the positions of the main peaks in the PEMD do not follow this formula because of a shift caused by the finiteness of $n_{\rm oc}$, which is another manifestation of the carrier-envelope phase effect.

IV. RESULTS AND DISCUSSION FOR THE HYDROGEN MOLECULAR ION

In this section, we apply the adiabatic theory to the analysis of PEMDs generated in strong-field ionization of the hydrogen molecular ion H_2^+. The geometry of the system is illustrated in the top left panel of Fig. 7. The nuclei are assumed to be located on the x axis in the polarization plane, symmetrically with respect to the origin. The interaction between the electron and the nuclei is modeled by the soft-core

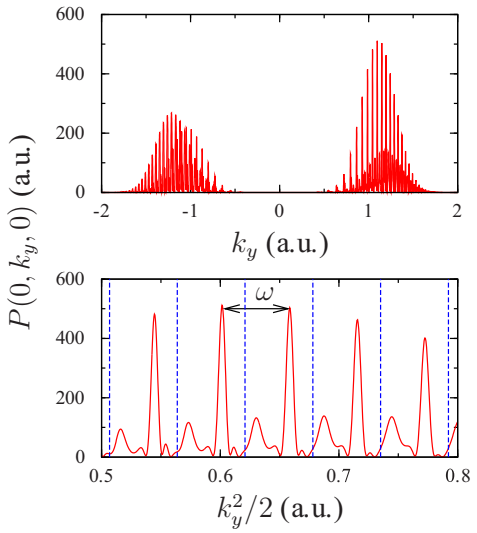

FIG. 6. One-dimensional cut along the k_y axis of the PEMD for H($1s$) generated by a pulse with $F_0 = 0.07$, $n_{oc} = 15$, and $T = 1650$ ($\omega \approx 0.057$) obtained from Eq. (6). The top panel shows the PEMD as a function of the photoelectron momentum k_y. The bottom panel reproduces the plot in the interval $1 \leqslant k_y \leqslant \sqrt{1.6}$, now as a function of the photoelectron energy $k_y^2/2$. Above-threshold ionization peaks separated by the photon energy ω are clearly seen in the latter format. The vertical dashed (blue) lines indicate the energies $k_y^2/2 = \mathrm{Re}[E(F_0)] - v_0^2/2 + n\omega$ where the peaks would be located for a monochromatic pulse in the limit $n_{oc} \to \infty$.

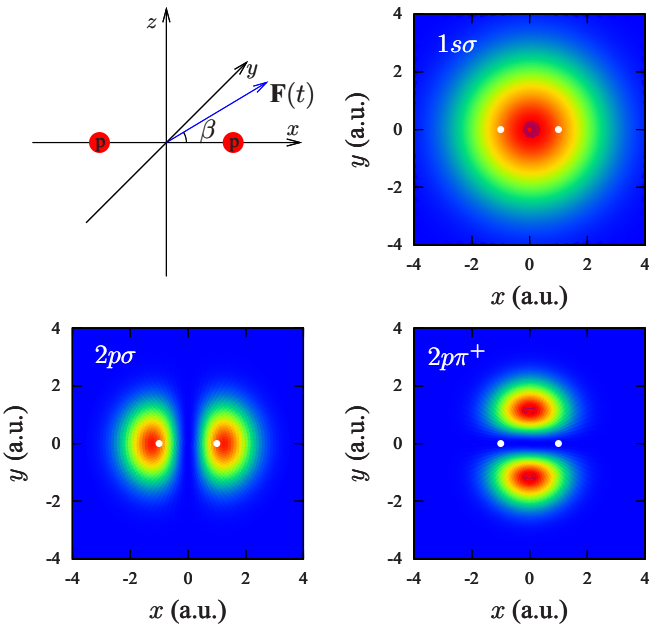

FIG. 7. Top left panel illustrates the geometry of the system. The nuclei are located on the x axis. The electric field vector $\mathbf{F}(t)$ lies in the polarization (x, y) plane under an angle β to the internuclear axis. The other panels show two-dimensional cuts in the polarization plane of the unperturbed electron densities $|\phi_0(\mathbf{r})|^2$ for the three states in the potential (17) considered in the calculations, with white circles indicating the positions of the nuclei. The energies of the states $1s\sigma$, $2p\sigma$, and $2p\pi^+$ in the present system are $E_0 = -0.962\,37$, $-0.555\,90$, and $-0.418\,95$, respectively.

potential

$$V(\mathbf{r}) = -\frac{1}{\sqrt{|\mathbf{r} - \mathbf{R}/2|^2 + a^2}} - \frac{1}{\sqrt{|\mathbf{r} + \mathbf{R}/2|^2 + a^2}}, \quad (17)$$

where $\mathbf{R} = (R, 0, 0)$, R is the internuclear distance, and a is a softening parameter. All the results reported below are obtained with $R = 2$ and $a = 0.3$. We consider ionization from three states (labeled by the united atom quantum numbers [49], with m denoting the projection of the electronic angular momentum onto the internuclear axis): the ground $1s\sigma$ state having no nodes, an excited $2p\sigma$ state having a node in the (y, z) plane, and an excited $2p\pi^+$ state given by a linear combination of the two degenerate $2p\pi$ states with $m = \pm 1$ which is even with respect to a reflection $z \to -z$ (this is indicated by the superscript $+$) and has a node in the (x, z) plane. Two-dimensional cuts in the polarization (x, y) plane of the unperturbed electron densities $|\phi_0(\mathbf{r})|^2$ for these states are shown in Fig. 7.

We wish to investigate how the shape of the initial orbital $\phi_0(\mathbf{r})$, in particular its nodal structure, is reflected in the shape of the PEMD. The PEMDs considered below are obtained from Eq. (6). The orbital properties appear in this formula through the SS energy eigenvalue $E(\mathbf{F})$ and the TMD amplitude $A(\mathbf{k}_\perp; \mathbf{F})$. For linear molecules, these properties as functions of the field $\mathbf{F}$ depend only on its strength F and the angle β between $\mathbf{F}$ and the internuclear axis (see Fig. 7). Note that, for given F and β, the TMD amplitude $A(\mathbf{k}_\perp; \mathbf{F})$ depends not only on the length $k_\perp$ of the transverse momentum, but also on its orientation in the plane perpendicular to $\mathbf{F}$; we define this orientation by a polar angle φ_k measured from the projection of the internuclear axis onto the plane. The behavior of these functions for the $1s\sigma$ and $2p\pi^+$ states in the present potential (17) was discussed and illustrated in Refs. [42,43]. Their relation to the structure of $\phi_0(\mathbf{r})$ becomes more transparent in the weak-field limit. For $F \to 0$, the Stark-shifted energy $\mathrm{Re}[E(\mathbf{F})]$ is given by the standard perturbation theory [46]; it affects the interference structure of the PEMD. The overall shape of the PEMD, which is of the main interest here, is determined by the functions $\Gamma(\mathbf{F})$ and $A(\mathbf{k}_\perp; \mathbf{F})$ describing the tunneling ionization process. These functions can be obtained from the WFAT as asymptotic expansions in F [44]. For the present system, the WFAT yields

$$\Gamma(\mathbf{F}) = \left[|G_{00}(\beta)|^2 + \frac{F}{2\varkappa^2}|G_{01}(\beta)|^2\right]\frac{\varkappa}{2}\left(\frac{4\varkappa^2}{F}\right)^{4/\varkappa - 1} \times \exp\left(-\frac{2\varkappa^3}{3F}\right) \quad (18)$$

and

$$A(\mathbf{k}_\perp; \mathbf{F}) = \left[G_{00}(\beta) - \frac{i}{\varkappa^{1/2}}G_{01}(\beta)k_\perp \cos\varphi_k\right]\frac{\pi^{1/2}}{2^{1/2}}\left(\frac{4\varkappa^2}{F}\right)^{2/\varkappa} \times \exp\left(\frac{2i\pi}{\varkappa} + \frac{i\pi}{4} - \frac{\varkappa k_\perp^2}{2F} - \frac{\varkappa^3}{3F}\right), \quad (19)$$

where $G_{00}(\beta)$ and $G_{01}(\beta)$ are the structure factors [50] in the state under consideration for the dominant and next-to-the-dominant ionization channels, respectively. These factors

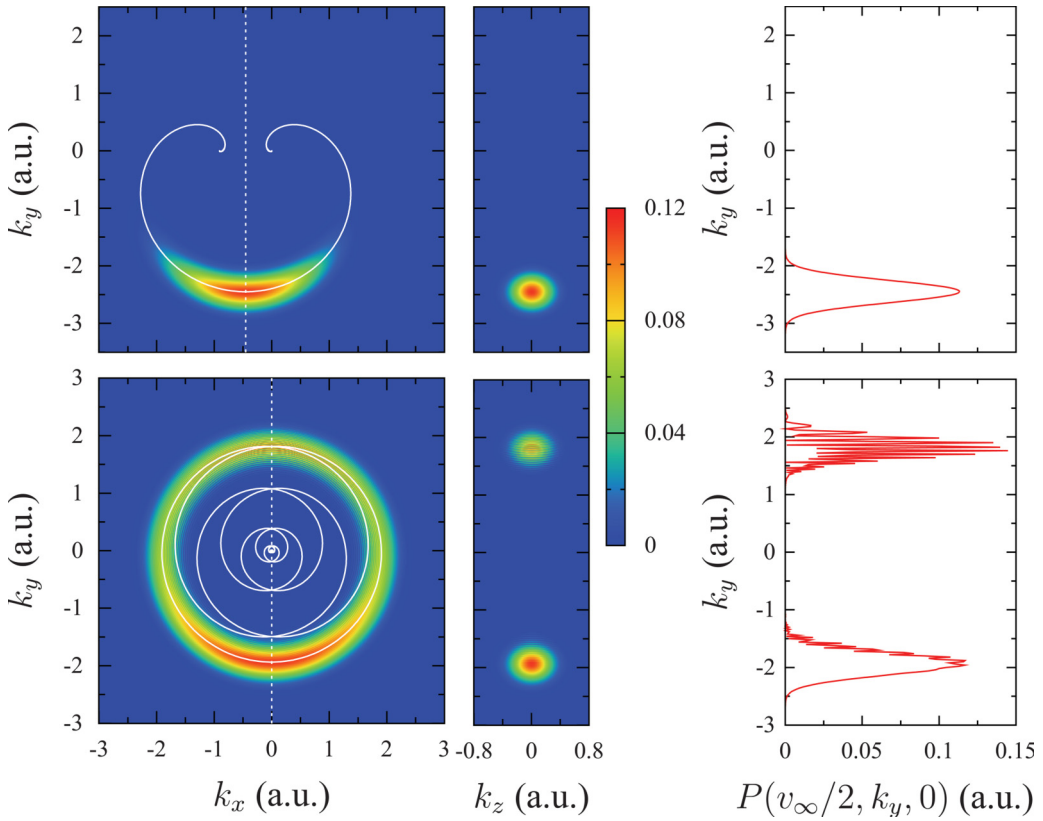

FIG. 8. Adiabatic results for PEMDs generated in the ionization of $H_2{}^+(1s\sigma)$ by pulses with $F_0 = 0.1$ and $\omega \approx 0.052$, hence, $v_0 \approx 1.91$. In the top panels, $n_{oc} = 1$ ($v_\infty \approx -0.90$) and $T = 120$. In the bottom panels, $n_{oc} = 4$ ($v_\infty \approx 0$) and $T = 480$. The left panels show two-dimensional cuts of the PEMDs in the plane $(k_x, k_y, k_z = 0)$. Here, the solid white lines show the curve $\mathcal{K}_a$ and the vertical dashed white lines indicate the position of $k_x = v_\infty/2$. The middle panels show two-dimensional cuts of the PEMDs in the plane $(k_x = v_\infty/2, k_y, k_z)$. The right panels show one-dimensional cuts of the PEMDs as functions of k_y along the white dashed lines in the left panels, that is, at $k_x = v_\infty/2$ and $k_z = 0$.

are determined by a coefficient in the projection of the unperturbed orbital $\phi_0(\mathbf{r})$ onto the corresponding parabolic channel function in the asymptotic region [44,50], and therefore reflect the structure of the orbital. In particular, $G_{00}(\beta)$ turns to zero in directions where $\phi_0(\mathbf{r})$ has a node; this is the case at $\beta = 90°$, for the $2p\sigma$ state, and at $\beta = 0°$ and $180°$, for the $2p\pi^+$ state. On the other hand, $G_{01}(\beta)$ turns to zero in directions around which $\phi_0(\mathbf{r})$ is axially symmetric; this is the case, e.g., at $\beta = 0°$ and $180°$ for $1s\sigma$ and $2p\sigma$ states. The first terms in the square brackets in Eqs. (18) and (19) containing $G_{00}(\beta)$ are the leading-order terms in the asymptotic expansions for $F \to 0$. The smallness of the second term in Eq. (18) is seen from the presence of an additional power of F. The second term in Eq. (19) does not contain such a factor explicitly. However, the TMD amplitude (19) as a function of $k_\perp$ is localized at $k_\perp \sim F^{1/2}$, which determines the width of the region K_a of localization of the PEMD around its classical support $\mathcal{K}_a$ in the weak-field case [51]. Thus, the second term in Eq. (19) contains an additional power of F implicitly in the factor $k_\perp$. Outside small intervals of the orientation angle β of size $\propto F^{1/2}$ around the zeros of $G_{00}(\beta)$, the second terms in Eqs. (18) and (19) represent small corrections which can be neglected, but near the zeros they become comparable with the leading-order terms and must be taken into account [43,50]. We will see that the interplay of the two terms in Eq. (19) in the latter case causes a modification of the transverse structure of the PEMD compared to the former case. Note that Eqs. (18) and (19) are consistent with Eq. (8). Let us recall that these equations are not exact; they hold only in the weak-field limit. The quantitative performance of the WFAT in the description of tunneling ionization in a static electric field from the $1s\sigma$ and $2p\pi^+$ states in the present model was illustrated in Refs. [42,43,52].

We will focus on two aspects of the donut-shaped PEMD: its longitudinal variation along the donut and its transverse structure in the different cross sections of the donut. According to Eq. (6), the coordinate in the photoelectron momentum space along the donut maps to the ionization time t, and hence to the angle β between the instantaneous electric field $\mathbf{F}(t)$ and the internuclear axis (see Fig. 7). For a nearly monochromatic pulse, the inner axis $\mathcal{K}_a$ of the donut is a circle of radius $v_0 = F_0/\omega$ lying in the polarization (k_x, k_y) plane with the center at the origin. As can be seen from Eq. (13), in this case each value of $0° \leqslant \beta \leqslant 180°$ corresponds to two points on $\mathcal{K}_a$, one in the region $k_x \geqslant 0$ and the other in the region $k_x \leqslant 0$. In particular, the points $(k_x, k_y) = (0, -v_0)$, $(v_0, 0)$, $(0, v_0)$, and $(-v_0, 0)$ on $\mathcal{K}_a$ correspond to $\beta = 0°$, $90°$, $180°$, and $90°$, respectively. The longitudinal variation of the PEMD is determined by the dependence of the ionization rate $\Gamma(\mathbf{F})$ on the orientation angle β, which in the weak-field case is

given by Eq. (18). On the other hand, cross sections of the donut at the different β are parametrized by the transverse momentum $\Delta\mathbf{k}_\perp$ defined by Eq. (15). The transverse structure of the PEMD is determined by the dependence of the TMD amplitude $A(\mathbf{k}_\perp;\mathbf{F})$ on $k_\perp$ and φ_k, which in the weak-field case is given by Eq. (19). In the calculations below we illustrate how the longitudinal variation and transverse structure of a PEMD reflect the structure of the initial orbital $\phi_0(\mathbf{r})$.

A. $1s\sigma$ state

We begin with the nodeless $1s\sigma$ state. PEMDs for this state generated by one-cycle and four-cycle pulses with $F_0 = 0.1$ and $\omega \approx 0.052$ are shown in the top and bottom panels of Fig. 8, respectively. The left panels in the figure present two-dimensional cuts of the PEMDs in the polarization $(k_x, k_y, k_z = 0)$ plane. We consider these cuts to discuss the longitudinal dependence of the PEMDs. For the one-cycle pulse, the PEMD as a function of the photoelectron momentum along $\mathcal{K}_a$ peaks at $\mathbf{k} = \mathbf{k}_a(0)$ (the point where $\mathcal{K}_a$ is crossed by the vertical dashed line in the figure) corresponding to the maximum of the pulse envelope (2) at $t = 0$. This longitudinal variation of the PEMD is mainly caused by the dependence of the ionization rate $\Gamma(\mathbf{F})$ on F and is revealed due to the smallness of the number of optical cycles in the pulse (the carrier-envelope phase effect); a similar behavior is seen in PEMDs generated by pulses with $n_{\rm oc} = 2$ shown in the left panels of Fig. 1. As $n_{\rm oc}$ grows, PEMDs for spherically symmetric atomic targets cease to depend on the coordinate along the donut; this is almost the case already for $n_{\rm oc} = 3$, as seen from Fig. 3. However, for molecular targets the situation is different. In the present case, the PEMD remains dependent on the coordinate along the donut even for nearly monochromatic pulses because the ionization rate $\Gamma(\mathbf{F})$ depends on β. This dependence reveals itself in the longitudinal variation of the PEMD for the four-cycle pulse shown in the bottom left panel of Fig. 8.

This feature is additionally illustrated in Fig. 9. The solid (black) line in the figure shows the exact ionization rate $\Gamma(\mathbf{F})$ of $H_2{}^+(1s\sigma)$ as a function of β for $F = 0.1$. For comparison, we have calculated the PEMD generated by a many-cycle ($n_{\rm oc} = 15$) pulse with $F_0 = 0.1$ and $\omega \approx 0.052$. The solid (red) circles in the figure are obtained by integrating this PEMD over the transverse momentum $\Delta\mathbf{k}_\perp$ across the donut at several values of β in the region $k_x \geqslant 0$; these results are normalized to the value of the rate at $\beta = 0^\circ$. The good agreement between the results demonstrates that the longitudinal variation of the PEMD for a many-cycle pulse reproduces the shape of the orientation dependence of the ionization rate. This conclusion is expectable, it follows from Eqs. (6) and (8) under the assumption that the depletion can be neglected, which is true in the present case. The numerical results presented in Fig. 9 confirm the conclusion and help to perceive it. Returning to the PEMD shown in the bottom left panel of Fig. 8, its minima at photoelectron momenta where the donut crosses the k_x axis reflect the minimum of the rate at $\beta = 90^\circ$. In addition, the leading-order WFAT results for the ionization rate are shown in Fig. 9 by the dashed (blue) line; these results are also normalized to the exact rate at $\beta = 0^\circ$. In the leading-order approximation, the WFAT rate (18)

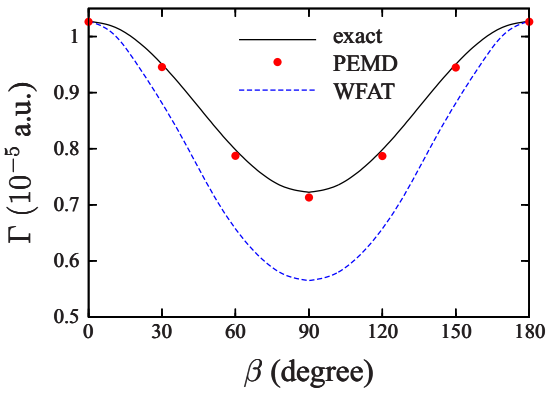

FIG. 9. Solid (black) line shows the exact ionization rate of $H_2{}^+(1s\sigma)$ as a function of the angle β between a static ionizing field $\mathbf{F}$ and the internuclear axis at the field strength $F = 0.1$. Solid (red) circles show results obtained by integrating the adiabatic PEMD from Eq. (6) generated by a pulse with $F_0 = 0.1$ and $\omega \approx 0.052$, as in Fig. 8, but for $n_{\rm oc} = 15$ and $T = 1800$, over the transverse momentum $\Delta\mathbf{k}_\perp$ across the donut at several values of β. Dashed (blue) line shows the structure factor squared $|G_{00}(\beta)|^2$ defining the orientation dependence of the leading-order WFAT results for the ionization rate. The PEMD and WFAT results are normalized to the exact rate at $\beta = 0^\circ$.

factorizes into the structure factor squared $|G_{00}(\beta)|^2$ and a field factor which does not depend on β, therefore, the dashed line in the figure reproduces the shape of $|G_{00}(\beta)|^2$ which is related to the shape of the initial orbital $\phi_0(\mathbf{r})$. Qualitatively, the orientation dependencies of the exact and WFAT rates have similar shapes, and in this sense one can say that the longitudinal variation of the PEMD reflects the shape of the orbital. However, only the exact rate reproduces the shape of the PEMD quantitatively, and this is related to the shape of the orbital in a less direct way. Within the WFAT, the difference is described by the first-order terms in the asymptotic expansion in F [52,53] which account for the Stark shift and distortion of the ionizing orbital by the field.

The middle panels in Fig. 8 show two-dimensional cuts of the PEMDs in the $(k_x = v_\infty/2, k_y, k_z)$ plane and the right panels present one-dimensional cuts along the line $(k_x = v_\infty/2, k_y, k_z = 0)$ shown by the vertical dashed lines in the left panels. These cuts illustrate the transverse structure of the PEMDs. For the present state, $G_{00}(\beta)$ never turns to zero, so the first term in Eq. (19) dominates at all β. In this case, the PEMD as a function of the transverse momentum $\Delta\mathbf{k}_\perp$ in cross sections of the donut at the different β has the same bell-like shape determined by the dependence of the exponential factor in Eq. (19) on $k_\perp$. The half-width of the bell can be estimated as $\Delta k_\perp \sim \sqrt{F_0/\varkappa}$, which in the present case gives 0.27. Inside the bell, there is a more or less pronounced interference substructure depending on the number of optical cycles in the pulse. This transverse structure of the PEMD is similar to that in the atomic case discussed in Sec. III. However, while in the atomic case the TMD amplitude does not depend on the angle φ_k defining the orientation of $\Delta\mathbf{k}_\perp$, there is such a dependence for molecular targets [43], that is, the bell is generally not symmetric, although for the present state the asymmetry is rather weak and not visible in the

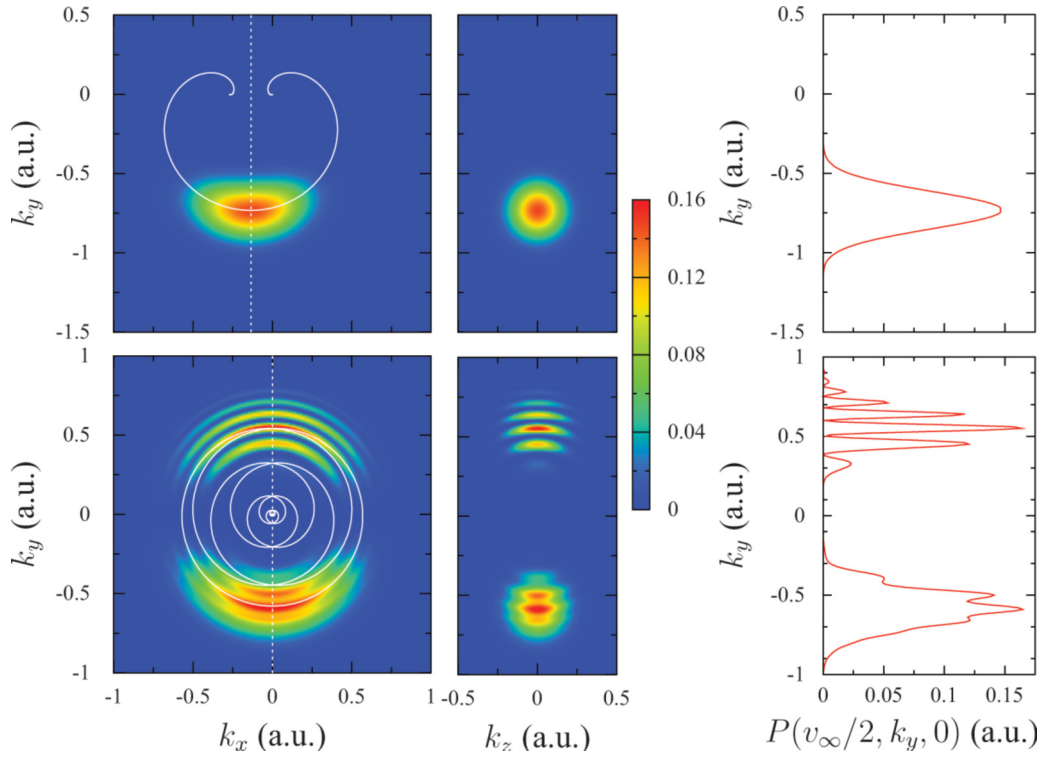

FIG. 10. Similar to Fig. 8, but for $H_2^+(2p\sigma)$. The PEMDs are generated by pulses with $F_0 = 0.03$ and $\omega \approx 0.052$, hence, $v_0 \approx 0.57$. In the top panels, $n_{oc} = 1$ ($v_\infty \approx -0.27$) and $T = 120$. In the bottom panels, $n_{oc} = 4$ ($v_\infty \approx 0$) and $T = 480$.

figure. Similar transverse structure of the PEMD is to be expected in the general case for arbitrary linear molecules in σ states in cross sections of the donut corresponding to orientation angles not close to zeros of the structure factor $G_{00}(\beta)$.

B. $2p\sigma$ state

We next discuss ionization from the $2p\sigma$ state. Figures 10 and 11 present results for this state similar to the results shown in Figs. 8 and 9. PEMDs generated by one-cycle and four-cycle pulses with $F_0 = 0.03$ and $\omega \approx 0.052$ are shown in the top and bottom panels of Fig. 10, respectively. The exact ionization rate $\Gamma(\mathbf{F})$ as a function of β for $F = 0.03$, the rate extracted from the PEMD generated by a many-cycle ($n_{oc} = 15$) pulse with $F_0 = 0.03$ and $\omega \approx 0.052$ by integrating it over the transverse momentum $\Delta\mathbf{k}_\perp$ at a given β, and the leading-order WFAT results for the rate are shown in Fig. 11. The main qualitative difference in the shape of the PEMDs from the previous case stems from the fact that the structure factor $G_{00}(\beta)$ for the $2p\sigma$ state turns to zero at $\beta = 90^\circ$ (see the WFAT results in Fig. 11), which reflects the node of the initial orbital in the (y, z) plane. This node explains the appearance of minima in the longitudinal dependence of the PEMD shown in the bottom left panel of Fig. 10 at photoelectron momenta where the donut crosses the k_x axis. The good agreement of the PEMD results in Fig. 11 with the ionization rate confirms the above conclusion that the variation of the PEMD along the donut reproduces the shape of the orientation dependence of the rate.

The middle and right panels in Fig. 10 demonstrate that the transverse structure of the PEMDs in cross sections of the donut at orientation angles β not close to the zero of $G_{00}(\beta)$ is determined by the first term in Eq. (19) and therefore is similar to the case of the $1s\sigma$ state. However, the situation near $\beta = 90^\circ$, where $G_{00}(\beta)$ turns to zero, is different. Note that the exact rate has a minimum at $\beta = 90^\circ$, it does not turn to zero there because of the second term in Eq. (18) (see Fig. 11).

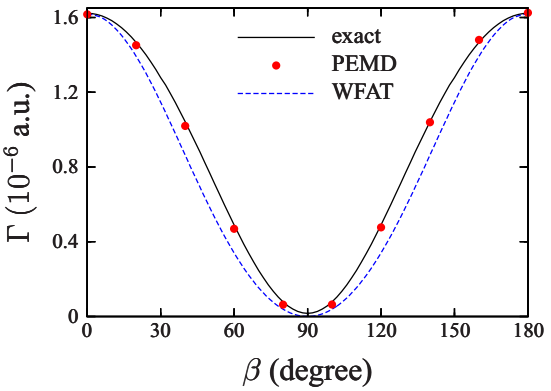

FIG. 11. Similar to Fig. 9, but for $H_2^+(2p\sigma)$. The exact rate is calculated for the field strength $F = 0.03$. The PEMD results are obtained by integrating the adiabatic PEMD from Eq. (6) generated by a pulse with $F_0 = 0.03$ and $\omega \approx 0.052$, as in Fig. 10, but for $n_{oc} = 15$ and $T = 1800$. Dashed (blue) line shows the structure factor squared $|G_{00}(\beta)|^2$. The PEMD and WFAT results are normalized to the exact rate at $\beta = 0^\circ$.

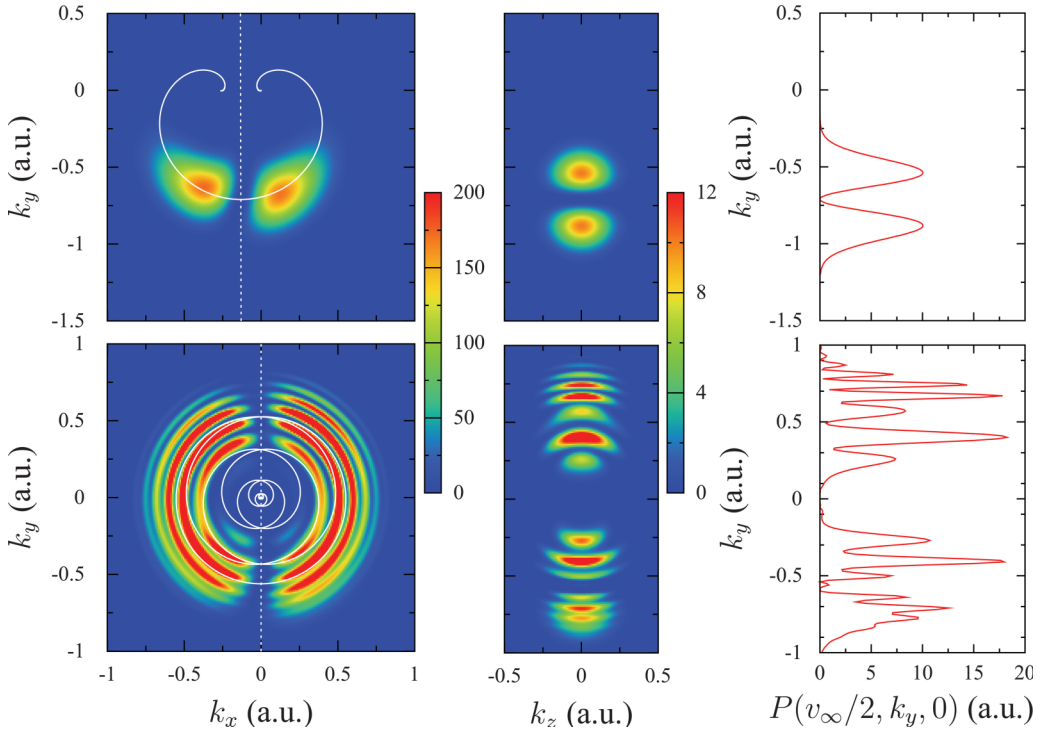

FIG. 12. Similar to Figs. 8 and 10, but for $H_2^+(2p\pi^+)$. The PEMDs are generated by pulses with $F_0 = 0.03$ and $\omega \approx 0.052$, hence, $v_0 \approx 0.57$. In the top panels, $n_{oc} = 1$ ($v_\infty \approx -0.27$) and $T = 120$. In the bottom panels, $n_{oc} = 4$ ($v_\infty \approx 0$) and $T = 480$.

At orientations near the zero of $G_{00}(\beta)$, the second term in Eq. (19) becomes comparable with the leading-order first term, which results in a rapid modification of the transverse structure of the PEMDs. We discuss this feature in more detail in the next subsection.

C. $2p\pi^+$ state

We finally discuss the $2p\pi^+$ state. Figures 12 and 13 present results for this state similar to the results shown in Figs. 8–11. PEMDs generated by one-cycle and four-cycle pulses with $F_0 = 0.03$ and $\omega \approx 0.052$ are shown in the top and bottom panels of Fig. 12, respectively. The exact ionization rate as a function of β for $F = 0.03$, the rate extracted from the PEMD generated by a many-cycle ($n_{oc} = 15$) pulse with $F_0 = 0.03$ and $\omega \approx 0.052$, and the leading-order WFAT results for the rate are shown in Fig. 13. The structure factor $G_{00}(\beta)$ for the $2p\pi^+$ state turns to zero at $\beta = 0^\circ$ and 180°. This explains deep minima in the longitudinal dependence of the PEMDs shown in the left panels of Fig. 12 at photoelectron momenta where the donut is crossed by the vertical dashed line [these are minima, not nodes, since the exact rate is not zero at $\beta = 0^\circ$ and 180° (see Fig. 13)]. One can also notice shallow minima in the PEMD shown in the bottom left panel of Fig. 12 where the donut crosses the k_x axis, which reflects the minimum of the exact ionization rate at $\beta = 90^\circ$ (see Fig. 13). The appearance of such a minimum in the ionization yield for $H_2^+(2p\pi^+)$ at $\beta = 90^\circ$ was also predicted by solving the TDSE [54]. This minimum results from the Stark shift and distortion of the initial orbital caused by the ionizing field. The leading-order WFAT does not account for these effects and therefore does not reproduce the minimum (see the dashed blue line in Fig. 13), but the inclusion of the first-order correction terms [53] within the WFAT does [52].

The transverse structure of the PEMDs in cross sections of the donut corresponding to the orientation angles $\beta = 0^\circ$ and 180° is shown in the middle and right panels of Fig. 12. The first term in Eq. (19) vanishes at these values of β. In small intervals of β near these orientations, where the first and second terms in Eq. (19) are comparable, the transverse structure

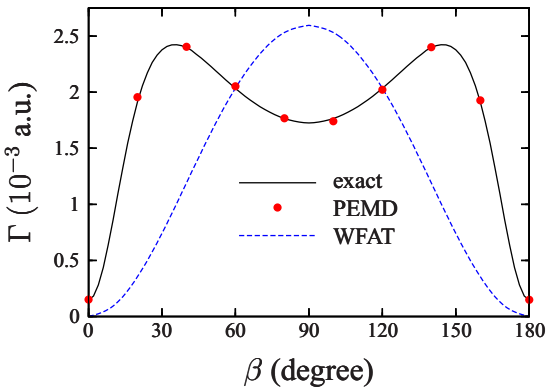

FIG. 13. Similar to Figs. 9 and 11, but for $H_2^+(2p\pi^+)$. The exact rate is calculated for the field strength $F = 0.03$. The PEMD results are obtained by integrating the adiabatic PEMD from Eq. (6) generated by a pulse with $F_0 = 0.03$ and $\omega \approx 0.052$, as in Fig. 12, but for $n_{oc} = 15$ and $T = 1800$. Dashed (blue) line shows the structure factor squared $|G_{00}(\beta)|^2$. The PEMD and WFAT results are normalized to the exact rate at $\beta = 60^\circ$.

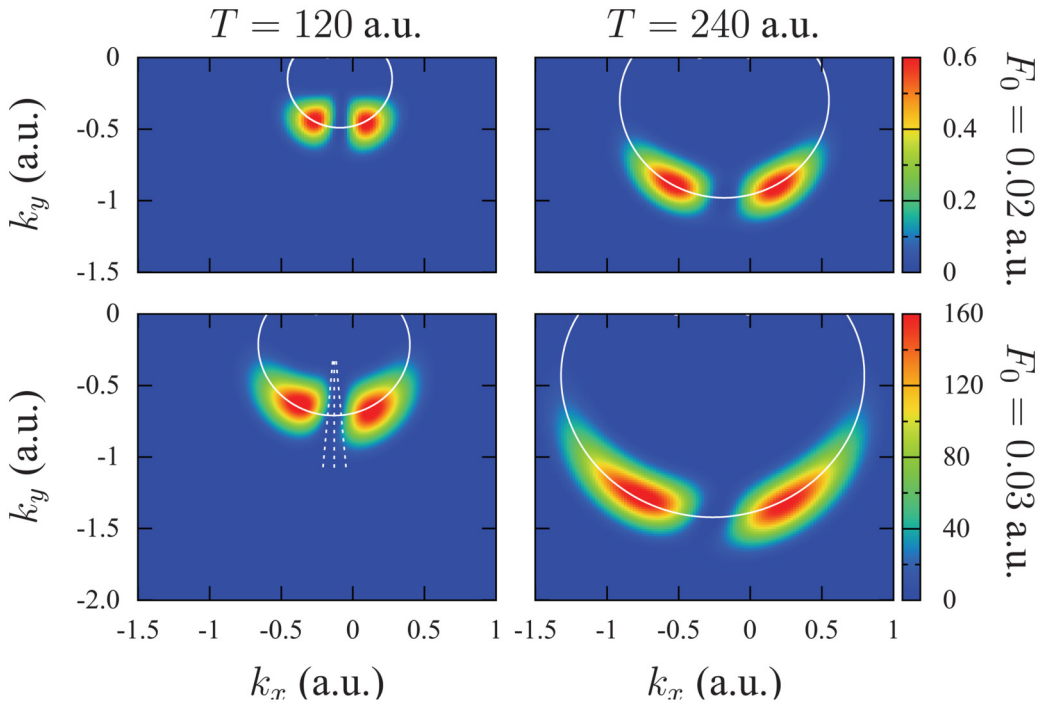

FIG. 14. Two-dimensional cuts in the polarization $(k_x, k_y, k_z = 0)$ plane of PEMDs for $H_2{}^+(2p\pi^+)$ generated by one-cycle pulses with durations T and amplitudes F_0 indicated in the figure. The solid white lines show the curve $\mathcal{K}_a$. The bottom left panel reproduces the results from the top left panel of Fig. 12.

of the PEMD is determined by the interplay of contributions from the two competing ionization channels. In the rest of this section we discuss the resulting structure in cross sections near $\beta = 0^\circ$ (in the lower part of the distributions in the left panels of Fig. 12) in more detail.

Let us first consider the PEMD generated by a one-cycle pulse shown in the top panels of Fig. 12. In this case, its transverse structure is not distorted by interference, so it is easier to understand it. The two-dimensional cut of the PEMD shown in the top middle panel of Fig. 12 corresponds to $\beta = 0^\circ$. At this β, the first term in Eq. (19) vanishes, so the structure seen in the figure is determined by the second term. This term as a function of the angle φ_k defining the orientation of $\Delta\mathbf{k}_\perp$ turns to zero at $\varphi_k = \pm\pi/2$, which results in the horizontal nodal line crossing the bell-like distribution shown in the figure. The nodal line is related to the minimum line seen in the lower part of the distribution in the top left panel of Fig. 12. One can notice that this line is not vertical, but slightly tilted. The tilting is additionally illustrated in Fig. 14, where we present two-dimensional cuts in the (k_x, k_y) plane of PEMDs generated by several one-cycle pulses with the different durations T and amplitudes F_0 indicated in the figure. The bottom left panel in Fig. 14 reproduces the results from the top left panel in Fig. 12. In all the cases, the minimum line in the lower part of the distributions is tilted, and the tilt angle is seen to grow with F_0. This feature is explained as follows. At $\beta = 0^\circ$, the nodal line in the transverse structure of the PEMD, which results from the $\cos\varphi_k$ factor in the second term in Eq. (19), passes through the center of the bell-like distribution, as in the top middle panel of Fig. 12. As β departs from 0°, the first term in Eq. (19) becomes nonzero. At small $|\beta|$, the nodal line still exists, but is shifted up (down) for positive (negative) β, because $G_{00}(\beta)$ changes sign at $\beta = 0^\circ$. This is illustrated in Fig. 15 showing the transverse structure of the PEMD from the bottom left panel of Fig. 14 in cross sections of the donut at $\beta = -5^\circ$, 0°, and 5° indicated by the dashed white lines. The middle panel in Fig. 15 reproduces the results from the top middle panel of Fig. 12; here, the nodal line passes through the center of the bell-like distribution. In the left and right panels of Fig. 15, it is shifted down and up, respectively, so the distribution restores its nodeless bell-like shape. The shift of the nodal line in the transverse structure of the PEMD caused by the interplay of the two terms in Eq. (19) results in tilting of the minimum lines in Fig. 14. As has been mentioned above (for details see Ref. [43]), the size of the interval of β where these terms are comparable is $\propto F^{1/2}$, so the tilt angle in Fig. 14 grows as F_0 grows.

The rapid modification of the transverse structure of PEMDs for linear molecules in π states in cross sections of the donut near $\beta = 0^\circ$ and 180° discussed above is an interesting feature which may provide an access to an additional structure information represented by the structure factor $G_{01}(\beta)$ for the next-to-the-dominant ionization channel. A question remains as to whether this feature survives contamination by interference and can be observed also in PEMDs generated by many-cycle pulses. The answer to this question is affirmative, as is demonstrated in Fig. 16. This figure shows one-dimensional cuts of the PEMD generated by a many-cycle ($n_{\rm oc} = 15$) pulse with $F_0 = 0.03$ and $\omega \approx 0.052$ as functions of $\Delta k_{\perp x} = \Delta k_\perp \cos\varphi_k$ along the line $k_z = 0$ in cross sections of the donut corresponding to the same three values of β as in Fig. 15. The solid (red) lines show the raw PEMD having a pronounced interference substructure. The dashed (blue) lines show the same results averaged over intervals of

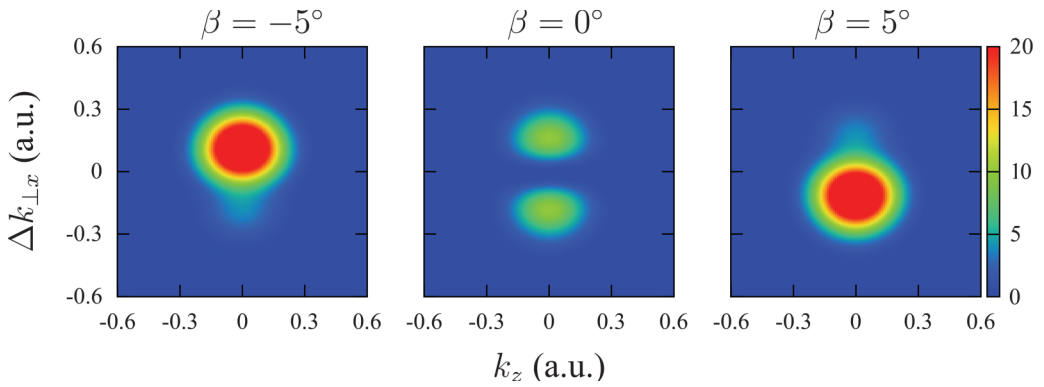

FIG. 15. Transverse structure of the PEMD for $H_2^+(2p\pi^+)$ shown in the top middle panel of Fig. 12 and the bottom left panel of Fig. 14 in cross sections of the donut corresponding to the three values of β indicated in the figure (these cross sections are shown by the dashed white lines in Fig. 14). The coordinates in the cross section plane are $\Delta k_{\perp x} = \Delta k_\perp \cos\varphi_k$ and k_z, where the transverse momentum $\Delta\mathbf{k}_\perp$ is defined by Eq. (15). The middle panel reproduces the results from the top middle panel of Fig. 12.

$\Delta k_{\perp x}$ of width 0.13. One can see that the maximum of the averaged distributions in the left and right panels is shifted towards positive and negative values of $\Delta k_{\perp x}$, respectively, while the distribution in the middle panel acquires a deep minimum at $\Delta k_{\perp x} = 0$. This behavior is consistent with the results shown in Fig. 15. Thus, the feature discussed above should be observable experimentally.

V. CONCLUSIONS

In this paper, we have investigated using the adiabatic theory [40] how the ionizing molecular orbital structure is imprinted in and can be extracted from donut-shaped strong-field PEMDs generated by circularly polarized laser pulses. The variation of the PEMD along the donut reproduces the orientation dependence of the ionization rate of the ionizing orbital which, in turn, reflects its nodal structure and shape. This conclusion is in accordance with the results presented, e.g., in Refs. [23,27,29]. Here, we have additionally shown that the longitudinal variation of the PEMD is related to the orbital through the structure factor $G_{00}(\beta)$ for the dominant ionization channel. Such structure factors have been tabulated for a number of diatomic molecules [55]. We have also analyzed the transverse structure of the PEMD in the different cross sections of the donut. It is shown that in cross sections near the ones corresponding to orientations of the molecule at which the ionizing orbital has a node in the direction opposite to that of the instantaneous laser field, the transverse structure of the PEMD undergoes a rapid modification reflecting the interplay of two competing ionization channels. This provides additional information on the orbital represented by the structure factor $G_{01}(\beta)$ for the next-to-the-dominant ionization channel. This analysis contributes to the understanding of how PEMDs generated by circularly polarized pulses can be used for imaging molecular orbitals and enables one to relate observable PEMDs to the shape of the ionizing orbital by means of the WFAT [44]. We believe its results will find applications in strong-field physics.

The analysis presented is based on the adiabatic theory [40]. Another result of the paper which is worth mentioning in view of future applications is that we have extended previous validations of this theory by comparison with TDSE results [9,40,45] to the case of strong-field ionization by circularly polarized pulses from Coulomb-tail potentials (Sec. III). The adiabatic theory is shown to quantitatively reproduce the TDSE results for the hydrogen atom and the agreement improves as the laser frequency decreases. We mention that quantitative performance of the adiabatic theory for many-electron systems has been recently demonstrated by comparison with experimental results on rescattering photoelectron spectroscopy of diatomic molecules NO and CO [10].

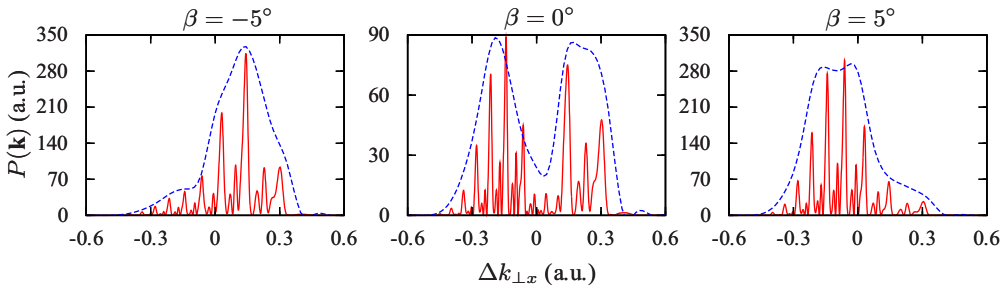

FIG. 16. Solid (red) lines show one-dimensional cuts of the PEMD for $H_2^+(2p\pi^+)$ generated by a pulse with $F_0 = 0.03$ and $\omega \approx 0.052$, as in Fig. 15, but for $n_{oc} = 15$ and $T = 1800$. The PEMD is shown as a function of $\Delta k_{\perp x} = \Delta k_\perp \cos\varphi_k$ at $k_z = 0$ in cross sections of the donut corresponding to the three values of β indicated in the figure. Dashed (blue) lines show the same results convoluted with a rectangular window function of width 0.13 and multiplied by a factor to fit the raw results.

To implement the adiabatic theory as prescribed [40], without further approximations, one needs to calculate the Siegert state corresponding to the ionizing orbital. In this paper, we have demonstrated the feasibility of such an accurate approach for diatomic molecules (Sec. IV) using molecular Siegert states calculated by the method of Refs. [42,43]. In principle, this technical development can be extended to larger molecules, however, the calculation of Siegert states in this case becomes more laborious. Alternatively, the adiabatic theory can be implemented more easily using the WFAT [44]. An error incurred by this approximation is illustrated by the difference between the solid (black) and dashed (blue) lines in Figs. 9, 11 and 13. The WFAT has been successfully applied to the analysis of strong-field ionization in experiments with diatomic [56], triatomic [57], and polyatomic [58–60] molecules. A general method to calculate structure factors for arbitrary polyatomic molecules needed for implementing the adiabatic theory has been developed recently [61,62]. This opens the way for applications of the theory to problems where solving the TDSE remains unfeasible, such as strong-field ionization of molecules by circularly polarized midinfrared laser pulses.

ACKNOWLEDGMENTS

This work was supported in part by Japan Society for the Promotion of Science KAKENHI Grants No. 16H04029, No. 16H04103, and No. 17K05597. V.N.T.P. acknowledges support from the Ministry of Education and Training of Vietnam under Grant No. B2018-SPS-20 and the Follow-up Research Fellowship from JASSO, Japan. O.I.T. acknowledges support from the Ministry of Education and Science of Russia (State Assignment No. 3.873.2017/4.6).

[1] F. Krausz and M. Ivanov, Attosecond physics, Rev. Mod. Phys. **81**, 163 (2009).

[2] J. Itatani, J. Levesque, D. Zeidler, H. Niikura, H. Pépin, J. C. Kieffer, P. B. Corkum, and D. M. Villeneuve, Tomographic imaging of molecular orbitals, Nature (London) **432**, 867 (2004).

[3] A. G. Ciriolo, M. Devetta, D. Faccialà, P. P. Geetha, A. Pusala, C. Vozzi, and S. Stagira, Molecular orbital tomography based on high-order harmonic generation: Principles and perspectives, in *Advances in the Application of Lasers in Materials Science*, edited by P. M. Ossi, Springer Series in Materials Science Vol. 274 (Springer, Cham, 2018).

[4] P. B. Corkum, Plasma Perspective on Strong-Field Multiphoton Ionization, Phys. Rev. Lett. **71**, 1994 (1993).

[5] G. G. Paulus, W. Becker, W. Nicklich, and H. Walther, Rescattering effects in above-threshold ionization: A classical model, J. Phys. B: At. Mol. Opt. Phys. **27**, L703 (1994).

[6] T. Morishita, A.-T. Le, Z. Chen, and C. D. Lin, Accurate Retrieval of Structural Information from Laser-Induced Photoelectron and High-Order Harmonic Spectra by Few-Cycle Laser Pulses, Phys. Rev. Lett. **100**, 013903 (2008).

[7] M. Meckel, D. Comtois, D. Zeidler, A. Staudte, D. Pavičić, H. C. Bandulet, H. Pépin, J. C. Kieffer, R. Dörner, D. M. Villeneuve, and P. B. Corkum, Laser-induced electron tunneling and diffraction, Science **320**, 1478 (2008).

[8] C. D. Lin, A.-T. Le, C. Jin, and H. Wei, Elements of the quantitative rescattering theory, J. Phys. B: At., Mol. Opt. Phys. **51**, 104001 (2018).

[9] T. Morishita and O. I. Tolstikhin, Adiabatic theory of strong-field photoelectron momentum distributions near a backward rescattering caustic, Phys. Rev. A **96**, 053416 (2017).

[10] Y. Ito, M. Okunishi, T. Morishita, O. I. Tolstikhin, and K. Ueda, Rescattering photoelectron spectroscopy of heterodiatomic molecules with an analytical returning photoelectron wave packet, Phys. Rev. A **97**, 053411 (2018).

[11] Y. Huismans, A. Rouzée, A. Gijsbertsen, J. H. Jungmann, A. S. Smolkowska, P. S. W. M. Logman, F. Lépine, C. Cauchy, S. Zamith, T. Marchenko, J. M. Bakker, G. Berden, B. Redlich, A. F. G. van der Meer, H. G. Muller, W. Vermin, K. J. Schafer, M. Spanner, M. Yu. Ivanov, O. Smirnova *et al.*, Time-resolved holography with photoelectrons, Science **331**, 61 (2011).

[12] Y. Zhou, O. I. Tolstikhin, and T. Morishita, Near-Forward Rescattering Photoelectron Holography in Strong-Field Ionization: Extraction of the Phase of the Scattering Amplitude, Phys. Rev. Lett. **116**, 173001 (2016).

[13] M. He, Y. Li, Y. Zhou, M. Li, W. Cao, and P. Lu, Direct Visualization of Valence Electron Motion Using Strong-Field Photoelectron Holography, Phys. Rev. Lett. **120**, 133204 (2018).

[14] H. Niikura, F. Légaré, R. Hasbani, A. D. Bandrauk, M. Yu. Ivanov, D. M. Villeneuve, and P. B. Corkum, Sub-laser-cycle electron pulses for probing molecular dynamics, Nature (London) **417**, 917 (2002).

[15] D. Pavičić, K. F. Lee, D. M. Rayner, P. B. Corkum, and D. M. Villeneuve, Direct Measurement of the Angular Dependence of Ionization for N_2, O_2, and CO_2 in Intense Laser Fields, Phys. Rev. Lett. **98**, 243001 (2007).

[16] H. Akagi, T. Otobe, A. Staudte, A. Shiner, F. Turner, R. Dörner, D. M. Villeneuve, and P. B. Corkum, Laser tunnel ionization from multiple orbitals in HCl, Science **325**, 1364 (2009).

[17] A. Staudte, S. Patchkovskii, D. Pavičić, H. Akagi, O. Smirnova, D. Zeidler, M. Meckel, D. M. Villeneuve, R. Dörner, M. Yu. Ivanov, and P. B. Corkum, Angular Tunneling Ionization Probability of Fixed-in-Space H_2 Molecules in Intense Laser Pulses, Phys. Rev. Lett. **102**, 033004 (2009).

[18] J. Wu, L. Ph. H. Schmidt, M. Kunitski, M. Meckel, S. Voss, H. Sann, H. Kim, T. Jahnke, A. Czasch, and R. Dörner, Multiorbital Tunneling Ionization of the CO Molecule, Phys. Rev. Lett. **108**, 183001 (2012).

[19] X. Wang, H. Xu, A. Atia-Tul-Noor, B. T. Hu, D. Kielpinski, R. T. Sang, and I. V. Litvinyuk, Isotope Effect in Tunneling Ionization of Neutral Hydrogen Molecules, Phys. Rev. Lett. **117**, 083003 (2016).

[20] S. X. Hu and L. A. Collins, Strong-field ionization of molecules in circularly polarized few-cycle pulses, Phys. Rev. A **73**, 023405 (2006).

[21] L. Holmegaard, J. L. Hansen, L. Kalhøj, S. L. Kragh, H. Stapelfeldt, F. Filsinger, J. Küpper, G. Meijer, D. Dimitrovski, M. Abu-samha, C. P. J. Martiny, and L. B. Madsen, Photoelectron angular distributions from strong-field ionization of oriented molecules, Nat. Phys. **6**, 428 (2010).

[22] L. Arissian, C. Smeenk, F. Turner, C. Trallero, A. V. Sokolov, D. M. Villeneuve, A. Staudte, and P. B. Corkum, Direct Test of

Laser Tunneling with Electron Momentum Imaging, Phys. Rev. Lett. **105**, 133002 (2010).

[23] C. P. J. Martiny, M. Abu-samha, and L. B. Madsen, Ionization of oriented targets by intense circularly polarized laser pulses: Imprints of orbital angular nodes in the two-dimensional momentum distribution, Phys. Rev. A **81**, 063418 (2010).

[24] J. L. Hansen, H. Stapelfeldt, D. Dimitrovski, M. Abu-samha, C. P. J. Martiny, and L. B. Madsen, Time-Resolved Photoelectron Angular Distributions from Strong-Field Ionization of Rotating Naphthalene Molecules, Phys. Rev. Lett. **106**, 073001 (2011).

[25] M. Odenweller, N. Takemoto, A. Vredenborg, K. Cole, K. Pahl, J. Titze, L. Ph. H. Schmidt, T. Jahnke, R. Dörner, and A. Becker, Strong Field Electron Emission from Fixed in Space H_2^+ Ions, Phys. Rev. Lett. **107**, 143004 (2011).

[26] D. Dimitrovski, M. Abu-samha, L. B. Madsen, F. Filsinger, G. Meijer, J. Küpper, L. Holmegaard, L. Kalhøj, J. H. Nielsen, and H. Stapelfeldt, Ionization of oriented carbonyl sulfide molecules by intense circularly polarized laser pulses, Phys. Rev. A **83**, 023405 (2011).

[27] J. L. Hansen, L. Holmegaard, L. Kalhøj, S. L. Kragh, H. Stapelfeldt, F. Filsinger, G. Meijer, J. Küpper, D. Dimitrovski, M. Abu-samha, C. P. J. Martiny, and L. B. Madsen, Ionization of one- and three-dimensionally-oriented asymmetric-top molecules by intense circularly polarized femtosecond laser pulses, Phys. Rev. A **83**, 023406 (2011).

[28] K.-J. Yuan and A. D. Bandrauk, Angle-dependent molecular above-threshold ionization with ultrashort intense linearly and circularly polarized laser pulses, Phys. Rev. A **84**, 013426 (2011).

[29] X. Zhu, Q. Zhang, W. Hong, P. Lu, and Z. Xu, Molecular orbital imaging via above-threshold ionization with circularly polarized pulses, Opt. Express **19**, 13722 (2011).

[30] J. Maurer, D. Dimitrovski, L. Christensen, L. B. Madsen, and H. Stapelfeldt, Molecular-Frame 3D Photoelectron Momentum Distributions by Tomographic Reconstruction, Phys. Rev. Lett. **109**, 123001 (2012).

[31] M. Spanner, S. Gräfe, S. Chelkowski, D. Pavičić, M. Meckel, D. Zeidler, A. B. Bardon, B. Ulrich, A. D. Bandrauk, D. M. Villeneuve, R. Dörner, P. B. Corkum, and A. Staudte, Coulomb asymmetry and sub-cycle electron dynamics in multiphoton multiple ionization of H_2, J. Phys. B: At. Mol. Opt. Phys. **45**, 194011 (2012).

[32] M. Busuladžić, A. Gazibegović-Busuladžić, W. Becker, and D. B. Milošević, Molecular above-threshold ionization with a circularly polarized laser field, Eur. Phys. J. D **67**, 61 (2013).

[33] I. Petersen, J. Henkel, and M. Lein, Signatures of Molecular Orbital Structure in Lateral Electron Momentum Distributions from Strong-Field Ionization, Phys. Rev. Lett. **114**, 103004 (2015).

[34] P.-L. He, N. Takemoto, and F. He, Photoelectron momentum distributions of atomic and molecular systems in strong circularly or elliptically polarized laser fields, Phys. Rev. A **91**, 063413 (2015).

[35] M. Abu-samha and L. B. Madsen, Alignment dependence of photoelectron momentum distributions of atomic and molecular targets probed by few-cycle circularly polarized laser pulses, Phys. Rev. A **94**, 023414 (2016).

[36] K. Liu and I. Barth, Nonadiabatic tunnel ionization of current-carrying orbitals of prealigned linear molecules in strong circularly polarized laser fields, Phys. Rev. A **94**, 043402 (2016).

[37] M. Murakami and Shih-I Chu, Photoelectron momentum distributions of the hydrogen molecular ion driven by multicycle near-infrared laser pulses, Phys. Rev. A **94**, 043425 (2016).

[38] K. Liu, K. Renziehausen, and I. Barth, Producing spin-polarized photoelectrons by using the momentum gate in strong-field ionization experiments, Phys. Rev. A **95**, 063410 (2017).

[39] M. Paul, L. Yue, and S. Gräfe, Strong-field ionization of asymmetric triatomic model molecules by few-cycle circularly polarized laser pulses, J. Mod. Opt. **64**, 1104 (2017).

[40] O. I. Tolstikhin and T. Morishita, Adiabatic theory of ionization by intense laser pulses: Finite-range potentials, Phys. Rev. A **86**, 043417 (2012).

[41] P. A. Batishchev, O. I. Tolstikhin, and T. Morishita, Atomic Siegert states in an electric field: Transverse momentum distribution of the ionized electrons, Phys. Rev. A **82**, 023416 (2010).

[42] L. Hamonou, T. Morishita, and O. I. Tolstikhin, Molecular Siegert states in an electric field, Phys. Rev. A **86**, 013412 (2012).

[43] V. N. T. Pham, O. I. Tolstikhin, and T. Morishita, Molecular Siegert states in an electric field. II. Transverse momentum distribution of the ionized electrons, Phys. Rev. A **89**, 033426 (2014).

[44] O. I. Tolstikhin, T. Morishita, and L. B. Madsen, Theory of tunneling ionization of molecules: Weak-field asymptotics including dipole effects, Phys. Rev. A **84**, 053423 (2011).

[45] M. Ohmi, O. I. Tolstikhin, and T. Morishita, Analysis of a shift of the maximum of photoelectron momentum distributions generated by intense circularly polarized pulses, Phys. Rev. A **92**, 043402 (2015).

[46] L. D. Landau and E. M. Lifshitz, *Quantum Mechanics (Non-relativistic Theory)* (Pergamon Press, Oxford, 1977).

[47] R. G. Newton, *Scattering Theory of Waves and Particles* (Springer, New York, 1982).

[48] T. Morishita, Z. Chen, S. Watanabe, and C. D. Lin, Two-dimensional electron momentum spectra of argon ionized by short intense lasers: Comparison of theory with experiment, Phys. Rev. A **75**, 023407 (2007).

[49] I. V. Komarov, L. I. Ponomarev, and S. Yu. Slavyanov, *Spheroidal and Coulomb Spheroidal Functions* (Nauka, Moscow, 1976).

[50] L. B. Madsen, O. I. Tolstikhin, and T. Morishita, Application of the weak-field asymptotic theory to the analysis of tunneling ionization of linear molecules, Phys. Rev. A **85**, 053404 (2012).

[51] N. B. Delone and V. P. Krainov, Energy and angular electron spectra for the tunnel ionization of atoms by strong low-frequency radiation, J. Opt. Soc. Am. B **8**, 1207 (1991).

[52] V. H. Trinh, V. N. T. Pham, O. I. Tolstikhin, and T. Morishita, Weak-field asymptotic theory of tunneling ionization including the first-order correction terms: Application to molecules, Phys. Rev. A **91**, 063410 (2015).

[53] V. H. Trinh, O. I. Tolstikhin, L. B. Madsen, and T. Morishita, First-order correction terms in the weak-field asymptotic theory of tunneling ionization, Phys. Rev. A **87**, 043426 (2013).

[54] G. L. Kamta and A. D. Bandrauk, Imaging electron molecular orbitals via ionization by intense femtosecond pulses, Phys. Rev. A **74**, 033415 (2006).

[55] R. Saito, O. I. Tolstikhin, L. B. Madsen, and T. Morishita, Structure factors for tunneling ionization rates of diatomic molecules, At. Data Nucl. Data Tables **103-104**, 4 (2015).

[56] T. Endo, A. Matsuda, M. Fushitani, T. Yasuike, O. I. Tolstikhin, T. Morishita, and A. Hishikawa, Imaging Electronic Excitation of NO by Ultrafast Laser Tunneling Ionization, Phys. Rev. Lett. **116**, 163002 (2016).

[57] H. Ohmura, N. Saito, and T. Morishita, Molecular tunneling ionization of the carbonyl sulfide molecule by double-frequency phase-controlled laser fields, Phys. Rev. A **89**, 013405 (2014).

[58] C. Wang, M. Okunishi, R. R. Lucchese, T. Morishita, O. I. Tolstikhin, L. B. Madsen, K. Shimada, D. Ding, and K. Ueda, Extraction of electron-ion differential scattering cross sections for C_2H_4 by laser-induced rescattering photoelectron spectroscopy, J. Phys. B: At. Mol. Opt. Phys. **45**, 131001 (2012).

[59] P. M. Kraus, B. Mignolet, D. Baykusheva, A. Rupenyan, L. Horný, E. F. Penka, G. Grassi, O. I. Tolstikhin, J. Schneider, F. Jensen, L. B. Madsen, A. D. Bandrauk, F. Remacle, and H. J. Wörner, Measurement and laser control of attosecond charge migration in ionized iodoacetylene, Science **350**, 790 (2015).

[60] S. G. Walt, N. B. Ram, A. von Conta, O. I. Tolstikhin, L. B. Madsen, F. Jensen, and H. J. Wörner, Role of multielectron effects in the asymmetry of strong-field ionization and fragmentation of polar molecules: The methyl halide series, J. Phys. Chem. A **119**, 11772 (2015).

[61] L. B. Madsen, F. Jensen, A. I. Dnestryan, and O. I. Tolstikhin, Structure factors for tunneling ionization rates of molecules: General Hartree-Fock-based integral representation, Phys. Rev. A **96**, 013423 (2017).

[62] A. I. Dnestryan, O. I. Tolstikhin, L. B. Madsen, and F. Jensen, Structure factors for tunneling ionization rates of molecules: General grid-based methodology and convergence studies, J. Chem. Phys. **149**, 164107 (2018).